Provided for non-commercial research and education use.
Not for reproduction, distribution or commercial use.

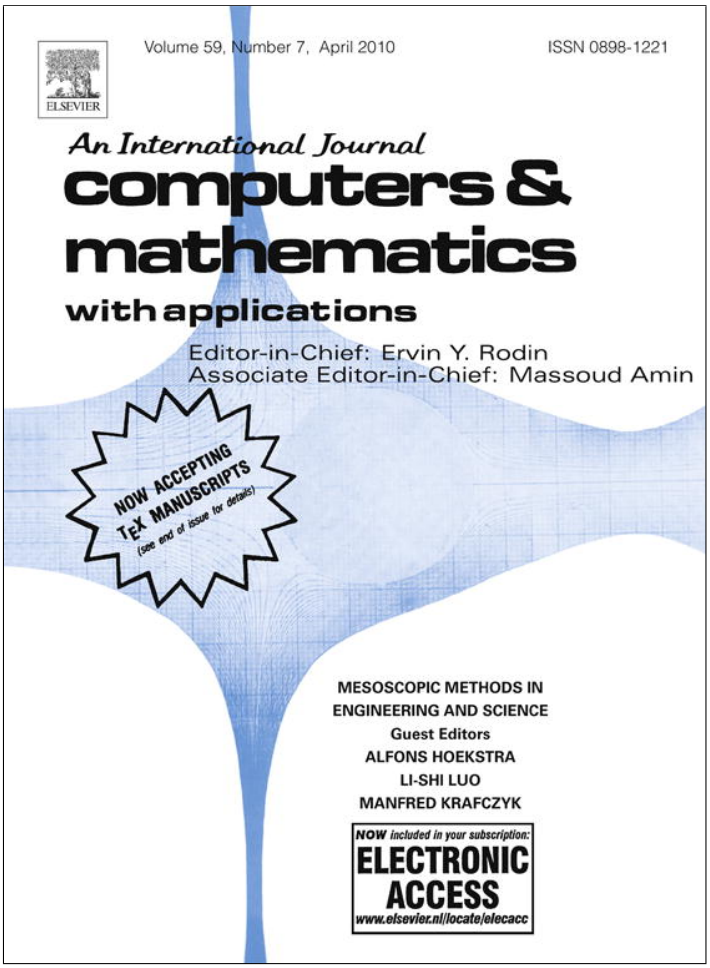

This article appeared in a journal published by Elsevier. The attached copy is furnished to the author for internal non-commercial research and education use, including for instruction at the authors institution and sharing with colleagues.

Other uses, including reproduction and distribution, or selling or licensing copies, or posting to personal, institutional or third party websites are prohibited.

In most cases authors are permitted to post their version of the article (e.g. in Word or Tex form) to their personal website or institutional repository. Authors requiring further information regarding Elsevier's archiving and manuscript policies are encouraged to visit:

http://www.elsevier.com/copyright

Author's personal copy

Computers and Mathematics with Applications 59 (2010) 2271–2289

Contents lists available at ScienceDirect

Computers and Mathematics with Applications

journal homepage: www.elsevier.com/locate/camwa

Three-dimensional microscale flow simulation and colloid transport modeling in saturated soil porous media

Hui Gao [a], Charmaine Q. Qiu [a], Dimin Fan [b], Yan Jin [b], Lian-Ping Wang [a,*]

[a] Department of Mechanical Engineering, University of Delaware, Newark, DE 19716, USA

[b] Department of Plant and Soil Sciences, University of Delaware, Newark, DE 19716, USA

ARTICLE INFO

Keywords:
Colloids
Colloid retention
Colloid transport
Lattice Boltzmann equation

ABSTRACT

Transport of sub-micron colloid particles in soil porous media has been mostly studied numerically with unit-cell-based grain-scale geometries. In this study, we develop a more general approach by combining a multiple-grain pore-scale flow simulation with Lagrangian tracking of individual colloids. First, two numerical methods are applied simultaneously to solve viscous flows in a channel partially or fully packed with spherical grain particles, this allows cross-validation of the numerical methods for considered model geometries. It is demonstrated that the mesoscopic lattice Boltzmann approach can more accurately simulate three-dimensional pore-scale flows with multiple grain–grain and grain–wall contact points. Colloid transport is simulated under the combined influence of hydrodynamic forces, Brownian force, and physicochemical forces. Preliminary results demonstrate the capture of colloids by the secondary energy minimum (SEM) well. The local hydrodynamic retardation is shown to reduce the ability for colloids to move into the SEM well, but does not prevent this. Trajectories before and after the capture are also discussed.

© 2009 Elsevier Ltd. All rights reserved.

1. Introduction

The attachment of colloids on grain surface and retention of colloids in small soil pores and their subsequent release when the solution or hydrodynamic conditions change determine the distribution and penetration of colloids in groundwater, and are important topics to groundwater contamination and remediation treatments. Most previous studies on colloid retention and transport address issues such as breakthrough curves at the macroscopic column scale. Research in recent years at the soil grain scale reveals that the retention and release depend on the competing effects of physicochemical and hydrodynamic forces acting on the colloids [1–3], indicating a need to better understand and model pore-scale flow in realistic three-dimensional (3D) porous media, particularly under unfavorable conditions as commonly encountered in natural porous media. Additionally, pore geometry affects local flow distribution and can contribute significantly to colloid retention. Important 3D flow features such as large local variations of flow velocity magnitude, direction, and shear rate depend on both grain–grain relative configuration and grain surface heterogeneity.

While the overall objective of our research is to develop an integrated experimental and computational approach focusing on pore-scale processes related to colloid transport [4,5], here we focus on developing a computational method to simulate the interaction of colloids with pore-scale flow and grain surfaces under various physicochemical and hydrodynamic conditions. In general, there are two components to pore-scale computational modeling: simulation of liquid flow and

* Corresponding author.
E-mail addresses: hgao@UDel.Edu (H. Gao), qiuqm@UDel.Edu (C.Q. Qiu), skyrock@udel.edu (D. Fan), yjin@udel.edu (Y. Jin), lwang@udel.edu (L.-P. Wang).

0898-1221/$ – see front matter © 2009 Elsevier Ltd. All rights reserved.
doi:10.1016/j.camwa.2009.08.057

Author's personal copy

simulation of transport of colloids by the liquid flow and interactions of colloid with grain surfaces. The second part could be performed in either an Eulerian or a Lagrangian fashion. The Eulerian approach solves a mean-field, extended advection–dispersion equation for colloid concentration [1,6]. The Eulerian approach requires a closure assumption of the driving source/sink terms and it is not certain if the approach can be applicable to unfavorable conditions where colloids and collectors are like-charged and thus are repulsive to one another.

The Lagrangian approach focuses on a single colloid and tracks its position and velocity over time according to Newton's second law. The colloid's equation of motion may include physicochemical, hydrodynamic, Brownian and body forces and torques. The physicochemical forces typically include contributions from the electrostatic, Lifshitz–van der Waals, and Lewis acid/base interactions [7]. The hydrodynamic forces may include Stokes drag, added mass, and fluid acceleration force. The hydrodynamic forces can be modified by a grain surface, nearby presence of other colloids, and local flow shear [8,9]. While the Lagrangian approach is computationally more expensive than the Eulerian approach, it provides a more direct mechanistic description of microscopic colloid transport. Furthermore, the discrete nature of the Lagrangian approach makes it much more feasible to include complex interactions with grain surface. For these reasons, most previous mechanistic modeling studies adopted the Lagrangian trajectory approach.

Under the Lagrangian trajectory approach, unit-cell-based flow representation were typically employed due to its computational efficiency. Examples include the sphere-in-cell model [8,10], 2D and 3D constriction tube models [11–14]. These unit-cell models provide a phenomenological representation of soil pore-scale geometry, but are unable to treat adequately grain–grain contact and grain surface irregularities. Cushing and Lawler [15] considered grain–grain contact in a unit cell representing densely packed regular array of spheres and solved the creeping fluid flow using an approximate Galerkin's method. They then studied colloid attachment efficiency using the trajectory approach. Johnson et al. [2] adopted the same unit-cell approach to solve pore-scale flow and a trajectory approach for colloids; they confirmed colloid retention in flow stagnation zones and wedging in grain-to-grain contacts. They also indicated the need to solve viscous flows through pore domains rendered from actual porous media, in order for such approach to become a useful quantitative tool.

Here we intend to study colloid transport and retention involving multiple grain–grain and grain–wall contacts in a model porous channel. To accurately simulate the pore-scale viscous flow, both the mesoscopic lattice Boltzmann method (LBM) and a Navier–Stokes-based hybrid method (i.e., Physalis) [4,16] are applied to same 3D flow configurations. The first part of this paper concerns inter-comparison of simulated 3D viscous flows in a channel. This extends the previous unit-cell flow representations. Simultaneous applications of two numerical methods provide a cross-validation step for simulating flows in the considered model geometry. Such inter-comparison has been performed recently for 2D pore-scale viscous flows by Gao et al. [4].

We then present a preliminary study of colloid transport in a simulated porous channel packed with 25 spherical grain particles (or glass beads). A preliminary study in 2D without considering local hydrodynamic interaction showed that the retention rate of colloids depends on both the mean flow speed and solution ionic strength [5]. Here we will extend our previous work to include local hydrodynamic interactions and 3D flow effects to more realistically model colloid transport and retention.

2. Flow simulation

In this section, we first introduce the two numerical methods for solving viscous flows in complex geometries. Several benchmark cases are then used to compare the results from the two methods. The general problem to be solved is flow through a three-dimensional channel with fixed spherical grain particles occupying part of the channel.

2.1. The mesoscopic lattice Boltzmann approach

The mesoscopic approach is based on a lattice Boltzmann equation with the multiple-relaxation-time (MRT) collision model using 19 discrete particle velocities in three dimensions (*i.e.*, the D3Q19 model), as described in detail in [17]. In the MRT-LBM, the evolution equation for the discrete particle density distribution function, f_i, for $i = 0,\ 1,\ 2, \ldots,\ 18$, is written as

$$f_i(\mathbf{x} + \mathbf{e}_i\delta_t, t + \delta_t) = f_i(\mathbf{x}, t) - M_{ij}^{-1}S_{jk}\left[m_k - m_k^{(\mathrm{eq})}\right] + \psi_i(\mathbf{x}, t), \tag{1}$$

where the collision operation is performed in a properly defined moment space through the transform matrix M_{ij} of rank 19×19, namely,

$$m_i = M_{ij}f_j, \qquad f_i = M_{ij}^{-1}m_j. \tag{2}$$

The detail of the transform matrix M_{ij} is given in [17]. By construction, the inverse matrix M_{ij}^{-1} can be easily obtained by the transpose of M_{ij} with a renormalization as the product of M_{ij} and its transpose is a diagonal matrix. In Eq. (1), ψ_i is a prescribed forcing field designed to model the driving pressure gradient or body force. In this work, ψ_i is specified as $\psi_i(\mathbf{x}, t) = \mathbf{e}_i \cdot \mathbf{F}_B/10$, where $\mathbf{F}_B$ is the macroscopic force per unit volume acting on the fluid. This forcing implementation is rather simple and does not explicitly consider the potential lattice effects associated with forcing, which has been described

Author's personal copy

in [18]. In this work, adequate lattice resolutions are always used and the lattice effects are assumed to be negligible, as demonstrated in [19]. Lallemand and Luo [20] suggested a two-step forcing implementation in the moment space, which is more consistent with the MRT-LBM model and should be used in our future simulations. The 19 discrete velocities in the D3Q19 model are ordered as

$$\mathbf{e}_i = \begin{cases} (0,0,0), & i = 0, \\ (\pm 1,0,0),\ (0,\pm 1,0),\ (0,0,\pm 1), & i = 1 \text{ to } 6, \\ (\pm 1,\pm 1,0),\ (\pm 1,0,\pm 1),\ (0,\pm 1,\pm 1), & i = 7 \text{ to } 18. \end{cases} \tag{3}$$

Specifically, the moment vector m_i contains four conserved elements, the density fluctuation $\delta\rho = \rho - \rho_0 = m_0$ and the flow momentum $(\rho_0 u_x, \rho_0 u_y, \rho_0 u_z) = (m_3, m_5, m_7)$. These conserved moments and the pressure field are calculated from f_i as

$$\delta\rho = \sum_i f_i, \qquad \rho_0 \mathbf{u} = \sum_i f_i \mathbf{e}_i, \qquad p = \delta\rho c_s^2, \tag{4}$$

where $\mathbf{u}$ is macroscopic fluid velocity, the sound speed c_s is $1/\sqrt{3}$ and the mean density ρ_0 is set to 1.0. The use of the density fluctuation instead of the total density in the above reduces the round-off error. The equilibria of all the non-conserved moments are related to $\delta\rho$ and $\rho\mathbf{u}$ [17]. The diagonal matrix $S = \text{diag}(s_0, s_1, \ldots, s_{18})$ specifies the relaxation rates of the non-conserved moments towards their respective equilibrium. The specific values used here are $s_0 = s_3 = s_5 = s_7 = 0$, $s_1 = 1.19$, $s_2 = s_{10} = s_{12} = 1.4$, $s_4 = s_6 = s_8 = 1.2$, $s_{16} = s_{17} = s_{18} = 1.98$, $s_9 = s_{11} = s_{13} = s_{14} = s_{15} = 1/(3\nu + 0.5)$, where ν is the kinematic fluid viscosity. Other details of the MRT-LBM model can be found in [17]. It should be noted that the previous single-relaxation-time LBGK model is recovered when all the relaxation rates are set to a same value. Recently, Ginzburg et al. [22,23] have developed a two-relaxation-time (TRT) LBM approach that is more efficient and suitable for viscous flow through porous media. This TRT-LBM could be used to find suitable choice of the various relaxation rates. The MRT-LBM has been shown to improve numerical stability at higher flow Reynolds numbers [17]. In our previous 2D pore-scale flow simulations [4], we found that MRT-LBM yields a more robust steady-state viscous flow solution for a wider range of relaxation parameter (or viscosity setting), when compared to the usual LBGK collision model.

A uniform cubic lattice is used to cover the computational domain. The straight channel walls are located in the middle of lattice links so a second-order accuracy is achieved with a simple bounce-back implementation. The inlet and outlet are also located half way on the lattice links to facilitate the implementation of the periodic boundary condition in the y direction.

The key implementation issue here is the treatment of solid particle surfaces. For each lattice node near a particle surface, we identify all links moving into the surface and their relative boundary-cutting location, namely, the percentage (α) of a link located outside the surface. Since particles are fixed, this information is pre-processed before the flow evolution. Before the streaming step, the missing population is properly interpolated in terms of α and two populations lying before and after the path of the missing population [21,24]. For results in this paper, we used the first-order interpolation based on two known populations, and found that the results are quite similar to the second-order interpolation based on three nodes [21]. The above simple interpolated bounce-back treatment represents a great advantage of LBM over traditional CFD approach. It handles complex boundary geometry using local lattice-link operations. All lattice nodes lying within the solid particles (including the fluid–solid interface) are excluded from LBE evolution, their velocities are simply set to zero. As a validation check, the total mass for the fluid nodes (excluding the fluid–solid interface nodes) is computed and found to essentially remain constant as time is advanced.

Another issue with the bounce-back interpolation is that two fluid lattice nodes may not be available when glass beads are in contact with one another or with channel walls. In this case, a simple one-node bounce back is used instead. This does not cause much problem as the fluid velocity near a contact point is typically very small.

2.2. The macroscopic hybrid approach: Physalis

To validate the mesoscopic LBM-MRT method, the same flow problems are also solved by a macroscopic Navier–Stokes-based hybrid approach (*i.e.*, Physalis) developed by Prof. Prosperetti and co-workers [16,25]. The basic idea for Physalis is to combine an analytical Stokes flow representation valid near the surface of spherical glass beads and the finite-difference numerical solution on the computational grid. Because of the no-slip boundary conditions on the surface, a glass bead induces a specific local flow structure that could be used to linearize the Navier–Stokes equations in the neighborhood of the glass-bead surface. The fluid velocity, pressure, and vorticity near the particle surface can be expressed analytically using series solutions of Stokes flow equations. As a result, the geometric surface of the particle can be replaced by a Stokes flow solution valid in a narrow but finite region near the surface, known as the cage region. A stair-case like interior boundary coinciding with the computational grid is defined by the inside face of the cage region, shown as the blue surface in Fig. 1.

The proper specification of the cage region and cage nodes requires a rather laborious effort for a sphere in three dimensions. Here we shall use Fig. 1 to illustrate the procedure. Three types of cage nodes are defined: the pressure cage nodes are located at cell centers, the velocity cage nodes at the centers of cell faces, and vorticity cage nodes at the centers of cell edges. The procedure for constructing the cage nodes and cage boundary is as follows. First, the pressure cage nodes are defined by identifying all cells whose centers are immediately inside the actual surface of a glass bead. A minimum set of such cells are used to define a connected interior boundary. The centers of this set of connected cells form the pressure cage nodes

Author's personal copy

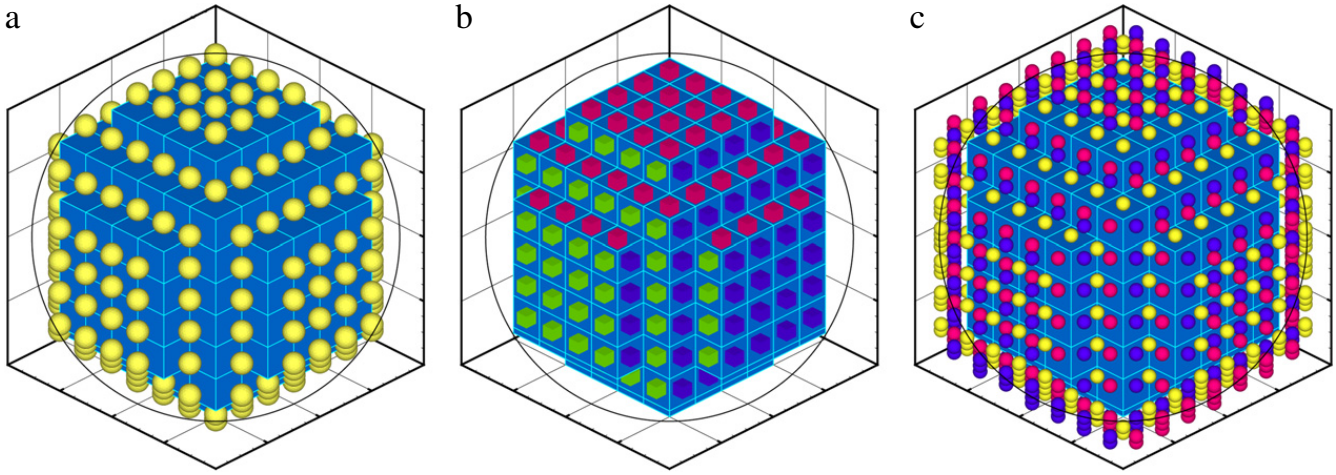

Fig. 1. Illustration of various cage nodes for a spherical glass bead centered at (8,8,8) with radius equal to 5. (a) pressure cage nodes are marked as yellow spheres; (b) green, blue and red cubes mark the location of velocity cage nodes in x, y, z directions, respectively; (c) red, blue and yellow spheres mark the location of vorticity cage nodes in x, y, z directions, respectively. Blue membrane represents the internal velocity boundary for all cases. (For interpretation of the references to colour in this figure legend, the reader is referred to the web version of this article.)

and, at the same time, the interior boundary is specified by connected interior cell faces of these connected cells (Fig. 1(a)). The spherical glass-bead surface is then replaced by the cage interior surface, in other words, the fluid region is virtually extended into a glass bead to the cage interior boundary. Second, the velocity cage nodes for all three velocity components are determined by using a combination of the boundary faces and cell surfaces that are normal to the interior boundary and immediately inside the interior boundary (Fig. 1(b)). These velocity cage nodes allow all fluid velocity nodes inside the extended fluid region to set up proper finite-difference equations according to the Navier–Stokes equation. Finally, the vorticity cage nodes are defined on all the edges of the pressure cage cells that are not located on the interior cage boundary (Fig. 1(c)). By this construction procedure, the pressure and vorticity cages nodes are typically within one grid spacing from the physical surface of the glass bead. While this procedure is described in [16], it took us a long time to set up the cage properly and validate the locations of the different types of cage nodes, in order to make sure that there is no hole in the cage region and there is no unnecessary redundancy.

When the cage nodes are set up, there are three main components in the hybrid method. The first component is an analytical representation of the flow within the cage region. This is obtained by the method of separation of variables applied to the linear Stokes flow equations. The general form in 3D can be found in Zhang and Prosperetti [16]. However, their paper contains several typos which have been corrected in our recent paper [26].

The second component is the numerical method for solving the Navier–Stokes equations on a regular staggered mesh (the flow solver). The second-order projection method [27] is used. The intermediate velocity in the fractional step procedure is solved by a factorization method [28], while the Poisson equation for the projection step is solved by a combination of transformation and tridiagonal inversion. The regular mesh extends to the interior of the particle surface. The velocity cage essentially defines an internal boundary for the viscous flow where the Stokes solution is employed to specify the boundary conditions there.

The most essential component is the coupling between the numerical solution on the regular mesh and the Stokes solution in the cage. This coupling is performed using pressure and vorticity at the pressure cage nodes and the vorticity cage nodes. This coupling is achieved by an iterative procedure in which (a) the numerical solution is used to refine the coefficients in the Stokes flow representation and in turn (b) the numerical solution is refined by an updated boundary conditions at the velocity cage from the refined Stokes flow. The first part is accomplished by a Singular Value Decomposition algorithm since an over-specified linear system is to be solved, namely, the number of pressure and vorticity cage nodes used for coupling is much larger than the number of coefficients. The second part currently relies only on the specific method of defining the cage velocity nodes or the internal boundary, so the analytical nature of the Stokes solution may not be fully taken advantage of.

Despite the complexity in constructing the cage nodes and in coupling the Stokes flow solution with numerical solution, an important advantage of this hybrid method is that the force and torque acting on the particle can be calculated directly from the expansion coefficients of the analytical Stokes solution, avoiding integration of the numerical solution over the glass-bead surface.

The fact that the pressure cage nodes are located completely inside the glass bead has the advantage of handling physical contact of two or more glass beads or contact of a glass bead with a channel wall. Here again, care is taken to make sure that no pressure or vorticity cage nodes from one glass bead are located in the interior of another glass bead or channel wall. Since currently a separate analytical Stokes flow must be constructed for each glass-bead surface, the method is not ideal for solving flow in a porous channel packed with many glass beads.

Author's personal copy

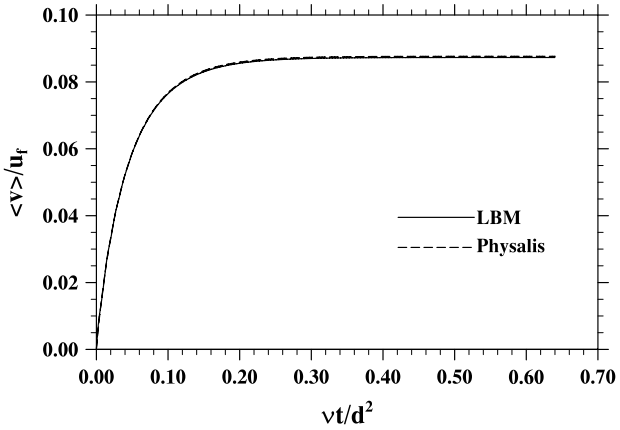

Fig. 2. The time evolution of mean velocity in the y direction, normalized by u_f, for $s = 9$.

Overall, the treatment of glass-bead surfaces in this macroscopic hybrid method is much more complex than the local interpolated bounce-back scheme in the LBM. As will be demonstrated in the next section, the accuracy of Physalis is deteriorated when many glass beads are in contact with one another or with channel walls.

2.3. Inter-comparison of simulated viscous flows in 3D porous channel

Our first goal is to ensure that the viscous flow in a 3D porous channel is accurately solved. This is achieved by establishing a good quantitative comparison between the results from LBM and Physalis. The inter-comparison of the two numerical methods includes the mean flow rate, local velocity profiles, as well as forces and torques acting on glass beads.

To proceed in a systematic manner, we consider three geometric settings below. In all cases, the y direction is the mean flow direction with a periodic length L so the computation domain covers $0 \le y \le L$. The channel cross-section has a width H in the x direction and a height W in the z direction. So $0 \le x \le H$ and $0 \le z \le W$. The body force $\mathbf{F}_B$ per unit volume used to drive the flow is expressed as $8\mu u_f/W^2$, where μ is the fluid dynamic viscosity and u_f is a characteristic fluid velocity if there were no glass beads in the channel.

2.3.1. Single glass bead in a square channel

The first general case involves a single fixed glass bead in the square channel of radius R. In terms of the grid spacing δ, $H = 100\delta$, $L = 80\delta$, $W = 80\delta$, and $R = 25\delta$. The center of the glass bead is located at $x = 42\delta$, $y = 40\delta$, and $Z = R + s\delta$, where s is a nearest gap distance between the glass-bead surface and the channel wall normalized by δ. The Reynolds number based on u_f is $Du_f/\nu = 2.5$ ($D = 2R$), but the Reynolds number based on the actual steady-state mean speed $\langle \mathrm{v} \rangle$ is about one order of magnitude smaller. The overall porosity in this case is 0.898.

Fig. 2 compares the simulated mean speed $\langle \mathrm{v} \rangle$ in the y direction, normalized by u_f, as a function of the dimensionless time $\nu t/D^2$, for $s = 9$. The steady-state values of $\langle \mathrm{v} \rangle/u_f$ are 0.08730 and 0.08766, for LBM and Physalis, respectively. In this case, the relative difference between the predicted mean flux is only 0.4%. We then reduce s to 3 and 0, the relative difference between the predicted mean flux becomes 0.37% and 0.35%, respectively. Therefore, regardless whether the glass bead touches the channel wall or not, the predicted mean flow speeds by LBM and Physalis are almost identical.

Since it is assumed that the fluid is at rest at $t = 0$, the body force then accelerates the flow. At the same time, the channel walls and the glass bead create resistance to the flow. The time it takes for the flow to reach to the steady state would be on the order of $\langle \mathrm{v}_\infty \rangle/(F_B/\rho_0) = 0.125(W/D)^2(\langle \mathrm{v}_\infty \rangle/u_f)(D^2/\nu) = 0.02794D^2/\nu$, where $\langle \mathrm{v}_\infty \rangle$ is the steady-state mean flow speed. The actual e-fold time based on Fig. 2 is about $1.7 \times 0.02794D^2/\nu$.

Fig. 3 shows the y-component velocity profiles at $z = 33.5\delta$ and three y locations. The line in Fig. 3(b) cuts through the glass bead and the surface locations of the glass bead are marked by the two horizontal lines. Since the z location is very close to the center of the glass bead, the blocking effect of the glass beads is shown at all three y locations. LBM and Physalis yield essentially the same velocity profile at each location.

Next we compare the force and torque acting on the glass bead in Table 1 for $s = 3$ and Table 2 for $s = 0$. The force on a glass bead is calculated by summing particle momentum changes along all boundary interaction lattice links, while torque is computed by summing the cross products of surface location vector and local momentum change, again along all lattice links. The detail for force and torque calculation can be found, for example, in Yu et al. [24]. The force components have been normalized by the net body force $\mathcal{F}_B = [LHW - 4\pi R^3/3]|\mathbf{F}_B|/\rho_0$, and the torque components by $\mathcal{F}_B R$. For $s = 3$, results from the two methods agree very well (to within 1% relative error), except for torque component in the y direction (Table 1). The y torque component is two to three orders of magnitude smaller than the other torque components, thus it is not surprising to observe a large relative error. For $s = 0$, again results from the two methods agree very well (Table 2), except for the torque component in the y direction (17.6% relative error) and the force component in the z direction (4.2%

Author's personal copy

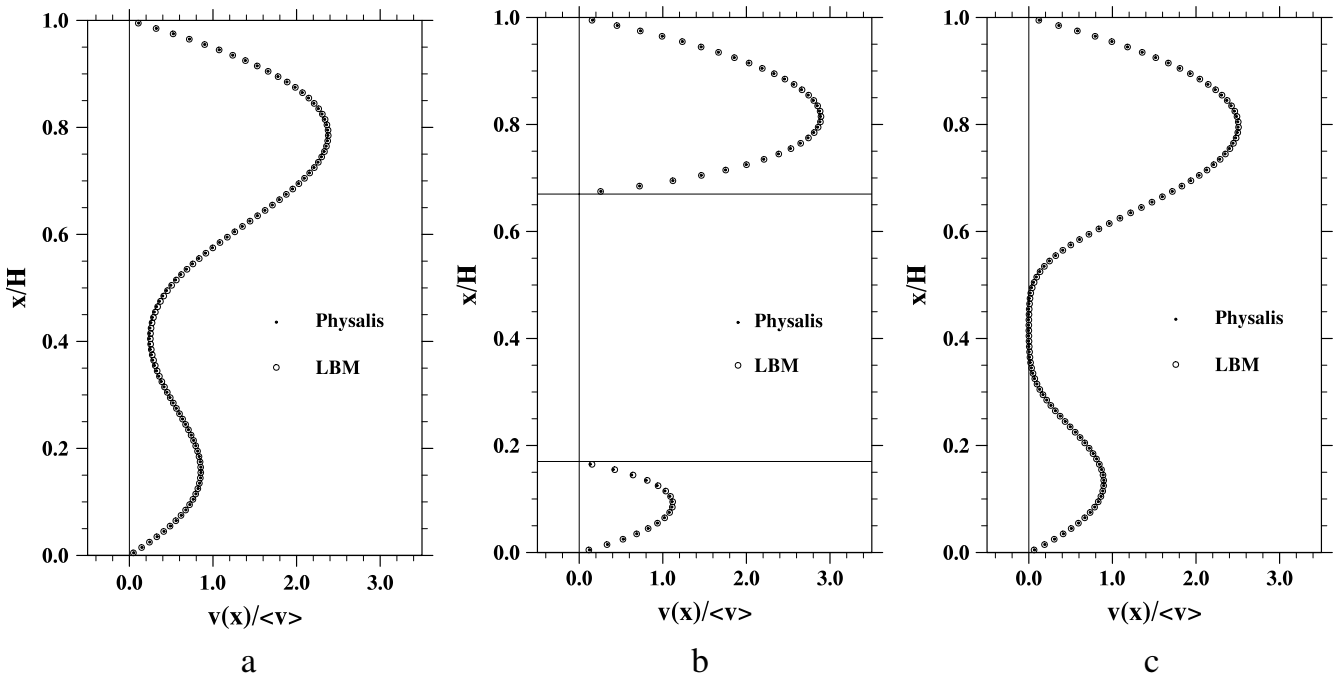

Fig. 3. Streamwise velocity profiles at $z = 33.5\delta$ and (a) $y = 0.5\delta$, (b) $y = 39.5\delta$, and (c) $y = 65.5\delta$.

Table 1
Normalized force and torque acting on the glass bead (Case 1, $s = 3$).

	$\langle v\rangle/u_f$	F_x	F_y	F_z	T_x	T_y	T_z
LBM	0.099308	0.0012552	0.36952	0.0013902	−0.065705	0.00011633	0.025717
Physalis	0.099678	0.0012486	0.37104	0.0013908	−0.066119	0.00013762	0.025892
R.E. (%)	0.37	0.53	0.41	0.05	0.64	18.3	0.68

Table 2
Normalized force and torque acting on the glass bead (Case 1, $s = 0$).

	$\langle v\rangle/u_f$	F_x	F_y	F_z	T_x	T_y	T_z
LBM	0.10811	0.0012265	0.36510	0.0025210	−0.082583	0.00014397	0.024909
Physalis	0.10848	0.0012190	0.36534	0.0026265	−0.084009	0.00016940	0.025053
R.E. (%)	0.35	0.61	0.07	4.18	1.73	17.6	0.58

relative error). This implies that the force in the wall normal direction may not be treated accurately as $s \to 0$, due to a strong pressure gradient in the local region near the contact point between the glass bead and the channel wall, when the glass bead touches the channel wall. Overall, LBM seems to be more accurate when the glass bead touches a channel wall. As another consistency check, we observe the following overall force balance at the steady state

$$\mathcal{F}_{\mathrm{GB}} + \mathcal{F}_{\mathrm{CW}} = \frac{\mathbf{F}_B}{\rho_0}\left[LHW - \frac{4\pi R^3}{3}\right], \tag{5}$$

where the two terms on the left hand side are force acting on the glass bead and force acting on the four channel walls, respectively; and the right hand side denotes the net body force, $\mathcal{F}_B$, acting on the fluid. The above balance was indeed observed in each method for each s value.

2.3.2. *Case 2: Two beads in a square channel*

Here we consider a case with two glass beads which both touch the channel walls and also touch each other in the plane $y = 0.5L$. The channel dimensions and glass-bead radius are identical to Case 1, the centers of the two glass beads are (0.25H,0.5L,0.3125W) and (0.65H,0.5L,0.6875W). The porosity for this case is 0.7955. Fig. 4 compares the time evolution of the normalized mean flow speed for this case. At the steady state, LBM and Physalis predict the value of $\langle \mathrm{v}\rangle/u_f$ to be 0.04248 and 0.04328, respectively, with Physalis giving a mean speed 1.87% larger than that of LBM. Again, the transition time to the steady state is on the order of $\langle \mathrm{v}_\infty\rangle/(F_B/\rho_0) = 0.125(W/D)^2(\langle \mathrm{v}_\infty\rangle/u_f)(D^2/\nu) = 0.01359D^2/\nu$. The actual e-fold time based on Fig. 4 is about $2.4 \times 0.01359D^2/\nu$. Note that the factor 2.4 here is larger than the corresponding factor 1.7 in Case 1, due to a more complex porous geometry in the channel.

Author's personal copy

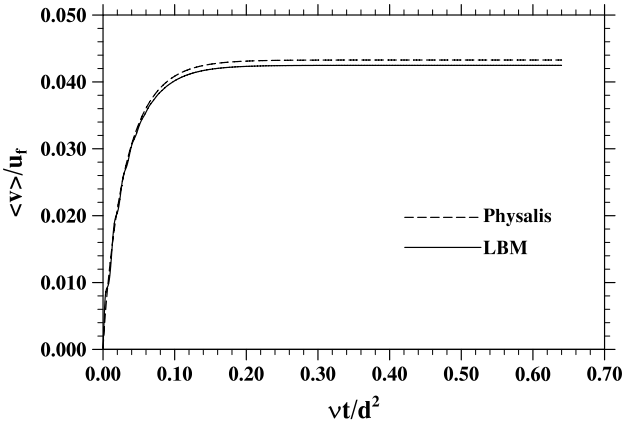

Fig. 4. The time evolution of the mean velocity in the y direction for the case with two glass beads. The results from LBM and Physalis have a relative error of 1.87%.

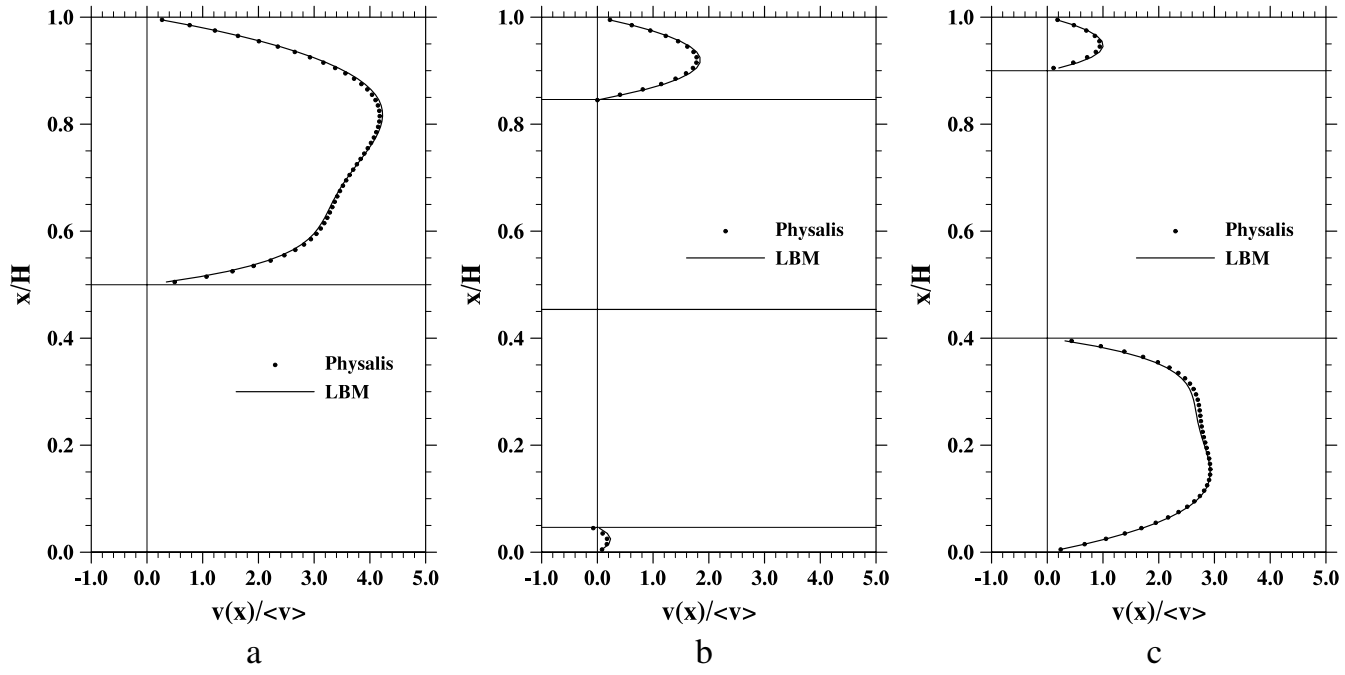

Fig. 5. Streamwise velocity profiles for Case 2 at $y = 39.5\delta$ and (a) $z = 24.5\delta$, (b) $z = 39.5\delta$, and (c) $z = 54.5\delta$. The lines show the results from LBM and symbols are the results from Physalis.

In Fig. 5 we compare the y component velocity profiles on three lines along the x direction. The glass-bead surfaces are marked with horizontal lines and only the velocity profiles in the fluid region is plotted. Overall, the velocity profiles agree well quantitatively, although some minor differences are visible in Fig. 5.

The total forces acting on glass beads and on channel walls are compiled in Table 3, and the sum is compared with the net body force. The last two columns of Table 3 are the relative error (defined as the difference between Physalis and LBM results, normalized by the LBM result) and the normalized error (defined as the force difference between Physalis and LBM, normalized by the net body force). The normalized error is less than 2%, indicating a reasonable comparison between the two methods. In LBM, overall balance as shown in Eq. (5) is observed precisely (Table 3). In Physalis, the sum of forces acting on the beads and walls is found to be 1.015 times the net body force, namely, there is a 1.5% relative error in Physalis on force balance. This suggests that LBM code is superior than the current version of Physalis code. This is likely due to the following reasons: (1) the coupling of Stokes flows and the numerical flow in Physalis becomes less accurate when there are particle–particle and particle–wall contacts; (2) since the force calculation in LBM is based on precise local momentum exchanges between the mesoscopic particles and a solid surface, the integral force balance follows more naturally in LBM.

2.3.3. Case 3: 25 beads in a square channel

In the last inter-comparison case, 25 glass beads are placed in the channel. The front and side views of the 25 glass beads relative to the channel are shown in Fig. 6. In this case, $L = 70\delta$, $H = W = 160\delta$, and $R = 20\delta$. Sixteen glass beads are

Author's personal copy

Table 3
Normalized forces and balance for Case 2. All forces are normalized by the net body force.

	LBM	Physalis	R.E. (%)	N.E. (%)
$\mathcal{F}_{GB}$:				
x	4.5587e−4	4.2787e−4	6.2	2.8e−3
y	5.6642e−1	5.8297e−1	2.9	1.7
z	−3.7450e−4	−3.7915e−4	1.3	4.7e−4
$\mathcal{F}_{CW}$:				
x	−4.5587e−4	−4.0881e−4	10.3	4.7e−3
y	4.3239e−1	4.3184e−1	0.13	5.5e−2
z	3.7451e−4	3.8574e−4	3.0	1.1e−3
$\mathcal{F}_{GB} + \mathcal{F}_{CW}$:				
x	0.000	1.91e−5	–	1.91e−3
y	0.9988	1.0148	1.6	1.6
z	0.00	6.59e−6	–	6.59e−4
$\mathcal{F}_B$:				
x	0.0	0.0	–	–
y	1.0	1.0	–	–
z	0.0	0.0	–	–

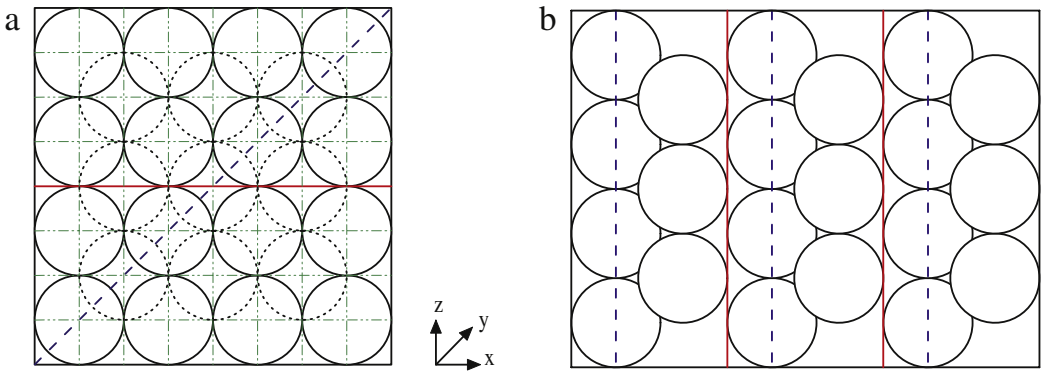

Fig. 6. Geometric configuration of 25 glass beads in 3D channel: (a) front (x–z) view; (b) side (y–z) view. This configuration is densely packed in the center of the cell, but not closely packed at the inlet and outlet.

located at $y = 20\delta$ and nine are at $y = 50\delta$. The porosity for this case is 0.5325. Again the flow is forced by a body force in the y direction with $F_B = 8\mu u_f / W^2$.

In both LBM and Physalis, $\nu = 1/9$ and $u_f = 0.2$. The simulated steady-state mean speed is $0.000521u_f$ in LBM, so the Reynolds number based on the mean speed and the diameter of the glass bead is $D\langle \mathrm{v} \rangle / \nu = 0.03733$. In the Physalis simulation, the simulated steady-state mean speed is $0.000589u_f$. Therefore, the mean flux in Physalis is 13.1% larger than the value in LBM. The reason for the larger flux in Physalis is partly due to the poor representation of no-slip boundary condition, as shown below.

Fig. 7 shows the velocity profiles for x and y components at $y = 0$ and $z = 0.5W$. Since this is a center cut at the inlet plane, by symmetry the z-component velocity is zero. On this particular line, there are three contact points (x/W = 0.25, 0.50, and 0.75) which are marked by the three horizontal lines. Both x- and y-velocity components are zero at these contact points. Fig. 7(b) shows clearly that LBM does better than Physalis in satisfying the no-slip boundary condition at the contact points. The y component velocity is larger than zero everywhere on the selected line, but the x component velocity takes both positive and negative value as the fluid finds its path through the gap regions in between the glass beads. LBM and Physalis give qualitatively similar profiles, both showing very complex velocity distributions. There are some quantitative differences between the LBM and Physalis results. The maximum y- component velocity is found near the channel wall as the local porosity is larger due to the unfilled space in the 9-bead layer.

The velocity distributions along a diagonal line ($x = z$) at the inlet plane are shown in Fig. 8. This time there are 7 glass-bead contact points as marked by the 7 horizontal lines. The LBM simulation gives zero value for all the three velocity components at the 7 contact points, but the y-component velocity in Physalis at the contact points (computed by interpolating from the numerical grid, not from the analytical Stokes flow) are not exactly zero. Due to the symmetry, the x-component and z-component velocity should have an identical profile. The LBM results meet this symmetry requirement, but the Physalis results do not meet this condition (not shown here). These observations plus a convergence test with varying mesh resolutions indicate that again LBM is better in handling viscous flow through a porous passage with many solid–solid contact points.

In summary, while LBM and Physalis yield almost identical results for a porous channel with one glass bead, the accuracy of Physalis appears to deteriorate as the number of glass beads (and contact points) is increased. In general, the local treatment of the no-slip boundary condition in LBM (interpolated bounce back) is not only simpler but also more accurate

Author's personal copy

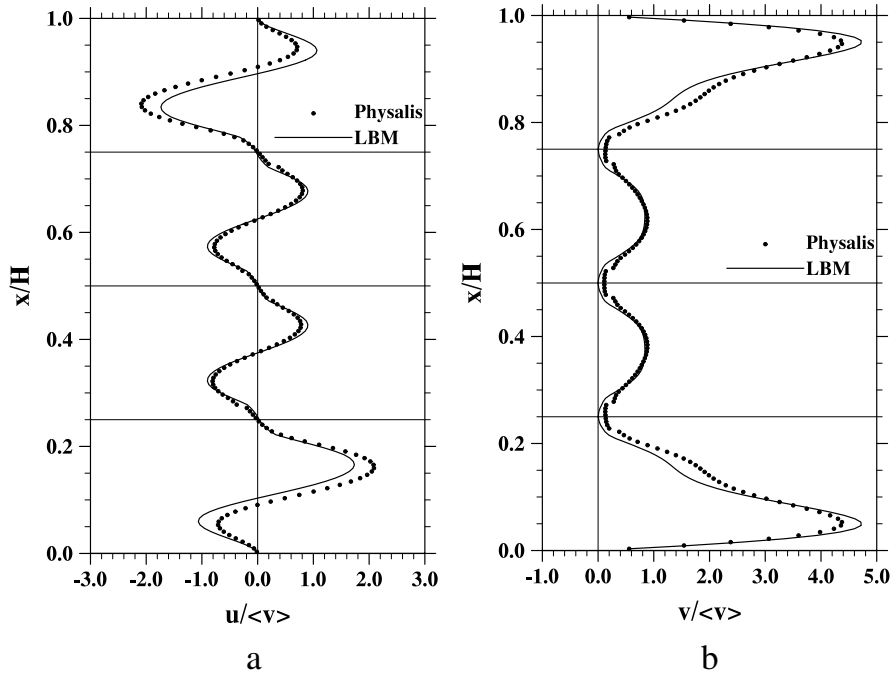

Fig. 7. (a) Velocity profiles at $y = 0$ and $z = 0.5W$: (a) u profile, (b) v profile. LBM simulation gives exact zero w velocity on the same line (not shown here), while Physalis yields a slightly non-zero value with magnitude below $0.6u_f \times 10^{-6}$.

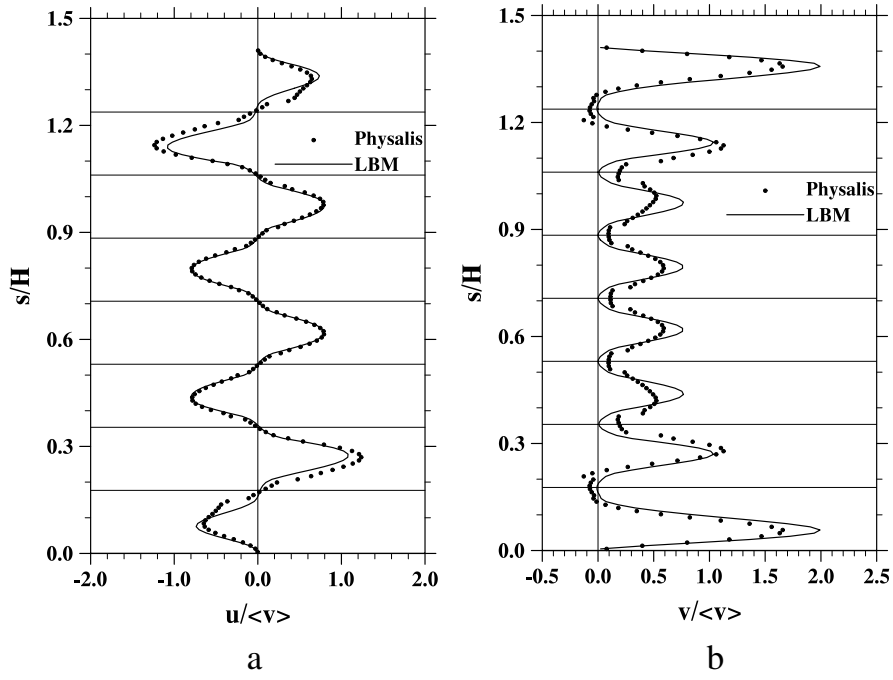

Fig. 8. Velocity profiles at $y = 0$ and along the diagonal line $z = x$: (a) u profile, (b) v profile.

than the whole-particle treatment in Physalis (via analytical Stokes flow solution on each glass bead). It may be possible that a higher mesh resolution is required for Physalis to accurately capture the very nonuniform flows in between the glass beads. In the following, the LBM flow is used when the transport of colloids is studied.

3. Transport of colloids

Now we consider a 3D porous medium flow through a square channel densely packed with spherical glass beads, as shown in Fig. 9. The glass beads were used in our parallel microscopic visualization [5]. The geometry is similar to Case 3 discussed in the last section, except that now even at the inlet and outlet the glass beads are packed. The flow simulation covers a region from the center of 25-bead layer to the center of the next 25 beads layer, as shown by the

Author's personal copy

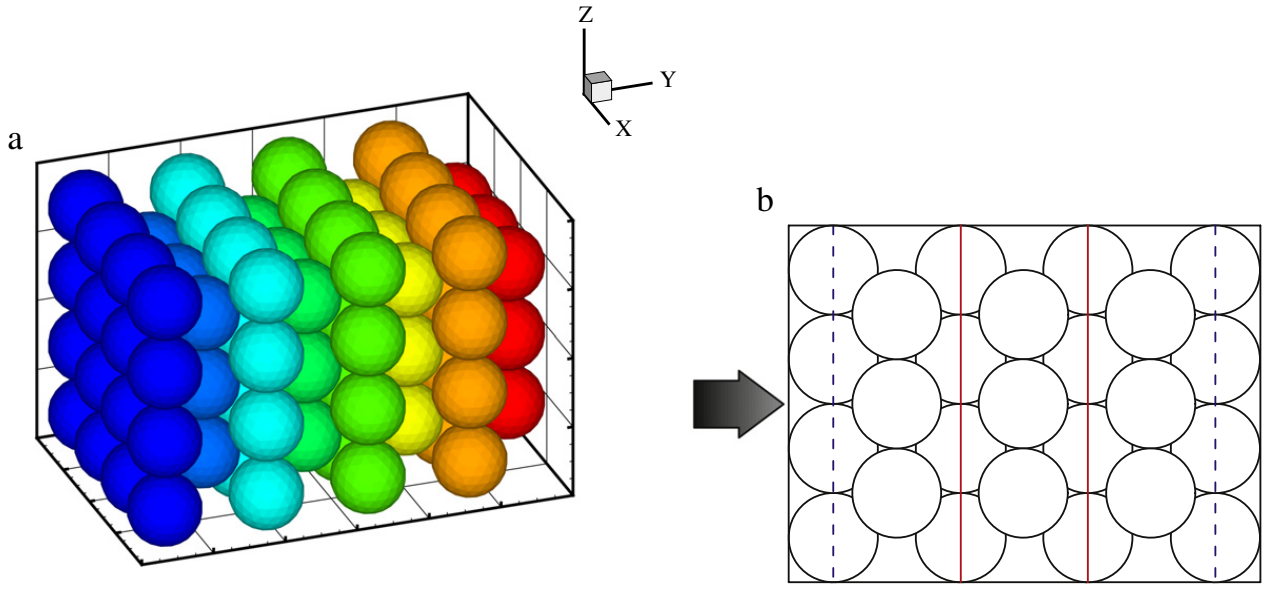

Fig. 9. A dense cubic packing of glass beads in a square channel used for preliminary colloidal transport study: (a) 3D view; (b) side view.

Table 4
Physical parameters and their values in the 3D numerical simulation.

	Symbol	Physical value	Value in simulation
water density	ρ	1000 kg/m^3	1
water viscosity	μ	0.001 kg/(m.s)	0.128
grid spacing	dx, dy	5 μm	1
channel width (/height)	H	800 μm	160
periodicity length	L	285 μm	57
glass-bead radius	R	100 μm	20
colloid radius	a_c	0.5 μm	0.1
velocity used in setting F_B	U_c	10 800 m/day	0.08
mean speed realized	U_s	3.52 m/day	2.608×10^{-5}
porosity	ϵ	0.426	0.426
nominal flow speed	U_s/ϵ	8.263 m/day	6.122×10^{-5}
colloid density	ρ_c	1055 kg/m^3	1.055
time step	dt	3.2×10^{-7} s	0.1
mass of colloid (actual)	m_c	5.524×10^{-16} kg	0.00442
mass of colloid (assumed)	m_c^*	6.033×10^{-12} kg	48.264
response time (actual)	τ_c	5.86×10^{-8} s	1.831×10^{-2}
response time (assumed)	τ_c^*	6.4×10^{-4} s	200
unit length		1.0 m	2.0×10^5
unit mass		1.0 kg	8.0×10^{12}
unit time		1.0 s	3.125×10^5
unit velocity		1.0 m/s	0.64
unit force		1.0 N	1.6384×10^7

two red solid lines in Fig. 9(b). The mesh resolution are set as: $H = W = 160\delta = 800$ μm, $L = 57\delta = 285$ μm, and $R = 20\delta = 100$ μm, where the mesh spacing is 5 μm (Table 4). The 16-bead layer is centered at $y = 0$ and the 9-bead layer at $y = 142.5$ μm. The nearest center-to-center distance between a bead in the 9-bead layer and a bead in the 16-bead layer is $\sqrt{142.5^2 + (100\sqrt{2})^2} = 200.764$ μm, so there is a tiny gap of 0.764 μm. Since this gap is much smaller than the grid spacing (5 μm) and is not resolved numerically, we may view that all beads are in contact with the nearby beads. The colloid diameter is 1 μm. The mean flow speed $\langle v \rangle \equiv U_s$, defined as the flux over the channel cross sectional area is 40.75 μm/s, which is designed to match a value of about 40 μm/s in our parallel experimental microscope visualization [5]. The ratio of $\langle v \rangle / u_f$ was found to be 3.26×10^{-4}. The flow Reynolds number based on this mean speed and glass-bead diameter is 0.00815. The porosity ϵ of the channel is 0.4259. The nominal flow speed, U_s/ϵ is about 8.26 m/day. Other parameters of the flow simulations are shown in Table 4.

3.1. Equation of motion for colloids

Colloids are randomly injected into the flow at the inlet plane ($y = 0$ plane) with initial velocity equal to the local flow velocity, and at a rate of about 260 colloids per second to simulate a number concentration of about 10^4 colloids per mm^3 water

Author's personal copy

solution. The velocity and location of each colloid are obtained by numerically integrating the equation of motion of the form

$$m_c \frac{\mathrm{d}\mathbf{V}(t)}{\mathrm{d}t} = \mathbf{F}^{\mathrm{drag}} + \mathbf{F}^{\mathrm{fa}} + \mathbf{F}^{\mathrm{am}} + \mathbf{F}^{\mathrm{b}} + \mathbf{F}^{\mathrm{g}} + \mathbf{F}^{\mathrm{B}} + \mathbf{F}^{\mathrm{c}}, \tag{6}$$

$$\frac{\mathrm{d}\mathbf{Y}(t)}{\mathrm{d}t} = \mathbf{V}(t) \tag{7}$$

where $\mathbf{V}(t)$ is the instantaneous (Lagrangian) velocity of the colloid, $m_c \equiv 4\pi\rho_c a_c^3/3$ is the mass of the colloid, ρ_c is the material density of the colloid, and a_c is the radius of the colloid. The hydrodynamic forces include the quasi-steady drag force $\mathbf{F}^{\mathrm{drag}}$, the fluid acceleration force $\mathbf{F}^{\mathrm{fa}}$, the added mass $\mathbf{F}^{\mathrm{am}}$. and the buoyancy force $\mathbf{F}^{\mathrm{b}}$. $\mathbf{F}^{\mathrm{g}}$ is the gravitational body force. $\mathbf{F}^{\mathrm{B}}$ is a random force designed to simulate Brownian motion of the colloid due to local thermal fluctuations of solvent molecules. Finally, $\mathbf{F}^{\mathrm{c}}$ represents interaction forces of the colloid with the glass (grain and wall) surface or other deposited colloids. An original derivation of the equation of motion can be found in [29]. The deviations relevant to the present application are explained below.

When a colloid is not close to a surface, the drag is the quasi-steady Stokes drag. However, when the distance between a colloid and a glass surface is on the order of colloid diameter, the drag force will be modified as a result of colloid–surface local hydrodynamic interaction [2,30]. Under the Stokes flow assumption, the flow field around a colloid near a surface can be solved. The net result of the colloid–surface hydrodynamic interaction is usually represented by a correction factor to the Stokes drag. It is convenient to consider these corrections in the directions normal and tangential to the surface separately. In the normal direction, the drag force may be written as

$$\mathbf{F}_n^{\mathrm{drag}} = \zeta \left(f_2 \mathbf{u}_n - \frac{\mathbf{V}_n}{f_1} \right) \tag{8}$$

where $\zeta \equiv 6\pi\mu a_c$, μ is the solvent viscosity, $\mathbf{u}_n = \left(\mathbf{u}\cdot\hat{n}\right)\hat{n}$, $\mathbf{V}_n = \left(\mathbf{V}\cdot\hat{n}\right)\hat{n}$, $\mathbf{u}(\mathbf{x}, t)$ is the Eulerian solvent velocity at the instantaneous location of the colloid, $\hat{n}$ is the unit normal vector pointing from the center of the nearest glass bead to the center of the colloid.

In the tangential direction, the drag force is

$$\mathbf{F}_t^{\mathrm{drag}} = \frac{\zeta}{f_4} \left(f_3 \mathbf{u}_t - \mathbf{V}_t \right) \tag{9}$$

where $\mathbf{u}_t = \mathbf{u} - \mathbf{u}_n$, $\mathbf{V}_t = \mathbf{V} - \mathbf{V}_n$.

The correction factors f_i are functions of $\bar{h}$, the gap distance, normalized by colloid radius, between the colloid surface and its nearest solid surface [2,30]:

$$f_1\left(\bar{h}\right) = 1.0 - 0.443\exp\left(-1.299\bar{h}\right) - 0.5568\exp\left(-0.32\bar{h}^{0.75}\right) \tag{10}$$

$$f_2\left(\bar{h}\right) = 1.0 + 1.455\exp\left(-1.2596\bar{h}\right) + 0.7951\exp\left(-0.56\bar{h}^{0.50}\right) \tag{11}$$

$$f_3\left(\bar{h}\right) = 1.0 - 0.487\exp\left(-5.423\bar{h}\right) - 0.5905\exp\left(-37.83\bar{h}^{0.50}\right) \tag{12}$$

$$f_4\left(\bar{h}\right) = 1.0 - 0.35\exp\left(-0.25\bar{h}\right) - 0.40\exp\left(-10.0\bar{h}\right). \tag{13}$$

These factors all reduce to 1 when $\bar{h}$ is larger than 3, and the Stokes drag is recovered.

The tangential direction is determined according to the sum of all tangential forces acting on the colloid, namely,

$$\hat{t} = \frac{\sum \mathbf{F} - \sum \mathbf{F}_n}{\left|\sum \mathbf{F} - \sum \mathbf{F}_n\right|}. \tag{14}$$

The fluid acceleration force is the force due to the background moving fluid and is given as

$$\mathbf{F}^{\mathrm{fa}} = m_f \frac{\mathrm{d}\mathbf{u}}{\mathrm{d}t} \tag{15}$$

where $m_f \equiv 4\pi\rho_f a_c^3/3$, ρ_f is the density of the fluid, and $\mathrm{d}\mathbf{u}/\mathrm{d}t$ is the fluid Lagrangian acceleration.

The added mass is a force due to the relative acceleration and is expressed as

$$\mathbf{F}^{\mathrm{am}} = -\frac{1}{2} m_f \left(\frac{\mathrm{d}\mathbf{V}}{\mathrm{d}t} - \frac{\mathrm{d}\mathbf{u}}{\mathrm{d}t} \right). \tag{16}$$

The buoyancy force and body force together is given as

$$\mathbf{F}^{\mathrm{bg}} = \mathbf{F}^{\mathrm{b}} + \mathbf{F}^{\mathrm{g}} = m_c \left(1 - \frac{\rho_w}{\rho_c} \right) \mathbf{g}, \tag{17}$$

Author's personal copy

where ρ_w is the solvent density and $\mathbf{g}$ is the gravitational acceleration.

The Brownian force is specified as $\mathbf{F}^{\mathrm{B}} = (F_1^{\mathrm{B}}, F_2^{\mathrm{B}}, F_3^{\mathrm{B}})$, where each component F_i^{B} is an independent Gaussian random variable of zero mean and the following standard deviation

$$\sigma_{F_i^{\mathrm{B}}} = \sqrt{\frac{2\zeta kT}{\mathrm{d}t}}, \tag{18}$$

where dt is the time step size, T is the temperature (assumed to be 293 K), $k = 1.38 \times 10^{-23}$ J/K is the Boltzmann constant. When a simple explicit Euler scheme is applied, the Brownian force would generate the desired mean square value (kT/m$_c$) of velocity fluctuation in each direction [31]. The ratio of the Brownian force to the drag force is estimated to be $\sqrt{2\tau_c kT/(m_c U_s^2 \mathrm{d}t)} \approx 2.84$, implying that the Brownian effect is as important as the drag force in transporting the colloidal particles. The above treatment for the Brownian motion is based on a stochastic (Langevin equation) model. It should be noted that an alternative method would be to directly introduce fluctuating hydrodynamics [32] within the lattice Boltzmann equation, known as the fluctuating lattice Boltzmann equation. This has been formulated in [33–35] and shown to yield correct thermal fluctuations. We adopted the particle-based Langevin equation approach since the pore-scale flow in the absence of thermal fluctuations was assumed to be steady and was solved first by MRT-LBM. It is important to note that in this work the disturbance flows near colloids are not directly resolved. The motion of colloids was then integrated via a modeled equation of motion, using a large number of time steps with a small time step size. A small time step size is necessary in view of a small inertial response time of colloid and rapid changes of hydrodynamic drag and electrostatic interaction force when a colloid is approaching a grain surface. On the other hand, the fluctuating lattice Boltzmann equation would require a simultaneous evolution of the pore-scale flow with thermal fluctuations and the motion of colloids without Brownian force. This could be computationally more expensive if a small time step size has to be used.

While the drag force and the Brownian force are active in all regions of the flow domain, the colloidal interaction force is only relevant when a colloid is very close to a solid surface or another deposited colloid. It consists of the electrostatic, Lifshitz–van der Waals, and Lewis acid/base interaction forces [36],

$$F^{\mathrm{c}} = F^{\mathrm{EDL}} + F^{\mathrm{LW}} + F^{\mathrm{AB}}, \tag{19}$$

where all interaction forces are assumed to act in the direction normal to a surface, with a positive value indicating a repulsive force and negative an attractive force. The formulation of these forces is primarily based on the Derjaguin–Landau–Verwey–Overbeek (DLVO) interaction potential [37,38]. The electrostatic double layer (EDL) force results from the interaction of a charged particle with the ions in the liquid medium. For colloid–glass surface interaction, the EDL force may be written as [5,39]

$$F^{\mathrm{EDL,cg}} = \frac{a_c \kappa}{1 - \exp(-2\kappa h)} \left[\alpha_1 \exp(-\kappa h) - \alpha_2 \exp(-2\kappa h)\right], \tag{20}$$

where h is the minimum gap between the colloid and a glass surface (the distance from the center of the colloid to the surface minus a_c), κ is the inverse Debye–Huckel screening length which depends on the solution ionic strength. Here we shall only consider an ionic strength at 100 mM in NaCl electrolyte solution, and in this case $1/\kappa = 0.963$ nm. The coefficients α_1 and α_2 are related to the surface potentials of the glass surface (-69.74 mV) and colloid (-76.99 mV) as well as the dielectric constant of the medium [5]. The surface potentials are computed based on the measured ζ-potentials (-41.31 mV and -45.56 mV, respectively) [5]. For the electrolyte solution used in this study [5], $\alpha_1 = 4.648 \times 10^{-11}$ N and $\alpha_2 = 4.671 \times 10^{-11}$ N. With the above parameters, the EDL force is repulsive and $F^{\mathrm{EDL}}/(\zeta U_s) > 1$ when $h/a_c < 0.02$ (Fig. 10). For the case of colloid–colloid interaction at 100 mM ionic strength, the EDL force is computed by [31]

$$F^{\mathrm{EDL,cc}} = (1.847 \times 10^{-11}\ \mathrm{N}) a_c \kappa \exp(-\kappa h), \tag{21}$$

where h is the minimum gap between the two approaching colloids.

The attractive Lifshitz–van der Waals (LW) interaction accounts for intermolecular interaction including London dispersion, Keesom dipole–dipole, and Debye induction. For the purpose of this paper, the LW force can be written as [5,36]

$$F^{\mathrm{LW}} = -\beta a_c \left(\frac{h_0}{h}\right)^2, \tag{22}$$

where h_0 is an equilibrium distance used to model the occurrence of physical contact and is set to 0.157 nm [31]. The constant β has been determined to be 0.0434 J/m^2 for colloid–surface interaction and 0.0469 J/m^2 for colloid–colloid interaction, based on the thermodynamic parameters of colloids, glass, and the liquid solution.

The Lewis acid/base (AB) force originates from the bonding reaction of a Lewis acid and a Lewis base. It can be expressed as [5,36]

$$F^{\mathrm{AB}} = -\gamma \frac{h_0 a_c}{\chi} \exp\left(\frac{h_0 - h}{\chi}\right), \tag{23}$$

Author's personal copy

Table 5
Force combinations tested in simulations of colloid transport and deposition.

	Brownian force	Local hydrodynamic interaction	Colloidal interaction force	Added mass	Fluid acceleration force	Gravity & buoyancy force
Run 1	ON	OFF	ON	ON	ON	OFF
Run 2	ON	ON	ON	ON	ON	OFF

Table 6
Number of deposited colloids and residence for different runs.

	PEM deposition (counts) ($h_{eq} = 0.157$ nm)	SEM deposition (counts) ($h_{gap} \lessapprox 13.3$ nm)	Near-surface residence (occurrence) ($h_{gap} < 13.3$ nm)	(13.3 nm $< h_{gap} < 100$ nm)
Run 1:	0 / 1000	93 / 1000	4.37×10^8	3.10×10^6
Run 2:	0 / 1000	43 / 1000	1.85×10^8	5.28×10^6

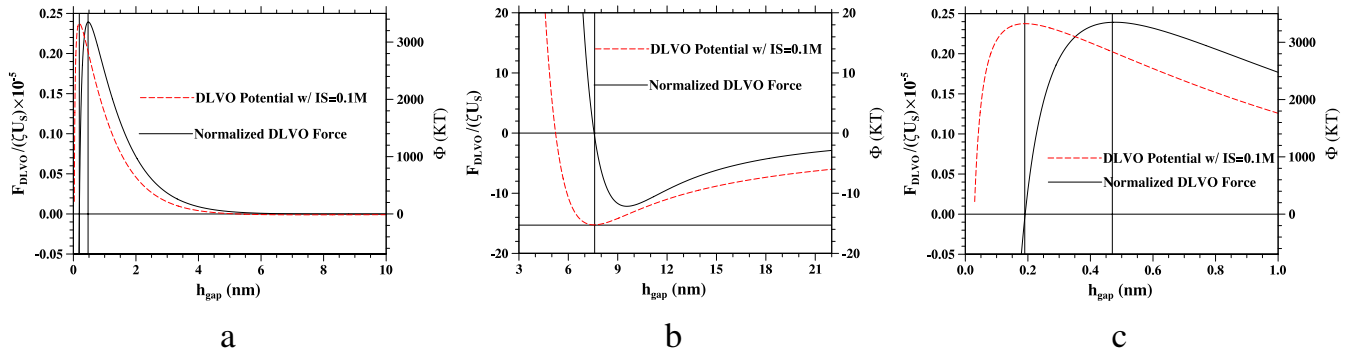

Fig. 10. DLVO potential energy and force as a function of the gap distance: (a) full view; (b) zoom-in view near SEM; (c) zoom-in view near peak energy barrier.

where $\chi = 0.6$ nm is the water decay length [36], the constant γ is determined, using the relevant electron-acceptor and electron-donor parameters, to be -0.0322 J/m^2 and -0.170 J/m^2 for colloid–surface and colloid–colloid interactions, respectively.

The numerical method for integrating the equation of motion follows our 2D simulations [4,5], namely, a fourth-order Adams–Bashforth scheme for colloid equation of motion excluding the Brownian force term, and Euler scheme for the Brownian force. Then the colloid location is updated by a fourth-order Adams–Moulton scheme. The time step size used to integrate the colloid equation of motion is $dt = 3.2 \times 10^{-7}$ s, thus one colloid is injected at the inlet every 12, 000 time steps. A total of 12 million time steps were calculated by the code, during this period 1000 colloids were injected and the injected fluid volume covers roughly 1.29 periodic lengths.

From Table 4, it is also noted that the flow time scale is on the order of $\tau_f = a_c/U_s = 0.0123$ s, therefore the Stokes number is $St = \tau_c/\tau_f = 4.764 \times 10^{-6}$, where $\tau_c = 2\rho_c a_c^2/(9\mu)$ is the inertial response time of a colloid. To reduce the stiffness of the colloid equation of motion, an adjusted colloid inertial response time τ_c^* was used (Table 4), leading to $St^* = \tau_c^*/\tau_f = 0.05203$ but still maintaining $St \ll 1$. A colloid is assumed to have deposited if the gap distance between the colloid surface and grain surface is less than 0.157 nm [5].

3.2. Results on colloid trajectories and retention

Here some preliminary results on transport and retention of colloids in 3D porous channel are discussed. Our main interest is to understand if and how a colloid will deposit on a solid surface (glass-bead surface and channel wall) when it is being transported through the porous flow passage.

Two runs (Table 5) were performed to isolate the effect of local hydrodynamic interactions. In Run 1 the hydrodynamic interactions were turned off by setting all the correction factors (f_1–f_4) to one. In Run 2, Eqs. (10)–(13) were used. The comparison of the two runs allows us to understand the role of local hydrodynamic interactions on colloid retention.

For each run, the simulation was repeated twice. First, only retention at the primary energy minimum (PEM) was counted by using a gap distance of 0.157 nm as the criterion for deposition. The gap distance 0.157 nm corresponds to the left of peak energy barrier (3324 kT located at 0.191 nm). The DLVO energy and force are shown in Fig. 10. For the specific conditions considered here, the peak energy barrier is extremely high, but the secondary energy minimum (SEM) is also significant, and the SEM well covers a larger region. The repeated run, while keeping all other conditions, used a gap distance of 13.3 nm as the retention criterion, namely, a colloid located below 13.3 nm at the end of simulation is viewed as a deposited colloid. 13.3

Author's personal copy

nm corresponds to a location with a negative energy potential of −10 kT, slightly to the right of secondary energy minimum (SEM, with DLVO energy of −15.25 kT at a gap distance of 7.58 nm). The idea here is that the first run captured retention at PEM only, while the second run capture both retention at both PEM and SEM. The differences between the numbers of retention from the two sub-runs may be loosely interpreted as the number of retention at SEM, as a retention at −10 kT location is likely to move further down to the SEM well and thus is unlikely to escape the SEM well — some evidence of this will be shown in Fig. 14(b) below. For the discussions below, the first sub-runs will be called Run 1a and Run 2a, and the repeated runs will be denoted as Run 1b and Run 2b.

Table 6 shows that the total number of deposited colloids at a time when a total of 1000 colloids have been injected at the inlet. No deposition was observed in both Run 1a and Run 2a, this is consistent with the very high (3324 kT) value of peak energy barrier.[1] Out of the 1000 colloids injected, 93 were found to be deposited at SEM when local hydrodynamic interactions were not considered. This number reduced to 43 when the hydrodynamic interactions (or hydrodynamic retardation effect) were included. This implies a factor of 2.2 reduction in deposition at SEM.

Also listed in Table 6 are the numbers of near-surface residence occurrence — an occurrence is counted if a colloid was found to be located within a selected gap distance range at any time step. Two gap distance ranges were considered: $h_{\text{gap}} < 13.3$ nm and 13.3 nm $< h_{\text{gap}} < 100$ nm. Interestingly, while the near-surface residence for $h_{\text{gap}} < 13.3$ nm was reduced to $1.85/4.37 = 42.3\%$ when the hydrodynamic retardation was introduced, the residence time for the gap range 13.3 nm $< h_{\text{gap}} < 100$ nm was 70% higher with the hydrodynamic retardation. This in part is due to slower velocity of a colloid in this region. Also a trapped colloid will also take longer time to escape this region. Taken together, the total residence times for $h_{\text{gap}} < 100$ nm were 7.47×10^8 and 7.13×10^8 for Run 1 and Run 2, respectively. In other words, the hydrodynamic retardation shifted colloids from the secondary energy well region to a region slightly outside (but still close to the grain surface). Note that the DLVO energy is −1.31 kT at 100 nm. Therefore, a portion of the colloids located in the range 13.3 nm $< h_{\text{gap}} < 100$ nm could still be viewed as temporarily deposited. We are working to generate local number concentration profile as a function of the gap distance, similar to what has been presented in Yang et al. [40] for an impinging jet system. This will require more samples (longer-time run) and more in-depth post-processing. Nevertheless, the above data implies that the concentration profile near the SEM is less peaked when the hydrodynamic retardation is considered.

We shall now examine some representative colloid trajectories. Fig. 11(a) shows 10 colloid trajectories within a y–z slice defined by $59\delta \le x \le 61\delta$ (i.e., a thickness of 10 μm). This slice contains the centers of the glass beads in the 16-beads layers. Although the slice is centered at the contact point of the 9-beads layer, the finite thickness of the slice implies a finite size of the 9-bead layer is intercepted, in this case, the projected radius is $\sqrt{100^2 - 95^2} = 0.312R$. More precisely, a range of interceptions from 0 to $0.312R$ are made, this is why a filled circle is drawn around the centers of the glass beads in the 9-beads layer. In contrast, the range of interceptions for the 16-beads layer is from R to $\sqrt{100^2 - 5^2} = 0.9987R$, so a thin line is drawn there. The x-axis points out of the paper. Each trajectory is marked by a different color and an identification number. A fixed time interval of 0.064 s is used to plot the locations of a colloid on a trajectory. Colloid 1 in Fig. 11(a) enters the cell in the negative x direction (such detail can only be obtained by zooming in the trajectory), then stays in the slice and moves along a curved streamline first upward (diverging streamlines seem in the y–z plane) then downward (converging in the y–z plane). When it approaches the converging zone, it gets deposited there (within SEM well). Most of the colloids (Colloids 2–7, and 10) find a more optimal flow region in between the glass beads and move more quickly (judged by the larger spacing between consecutive locations). In fact, they leave the slice temporally to avoid the strong convergence zone in the slice and re-enter the slice at a later time. Colloid 8 travels very slowly near the contact point in the 9-beads layer but eventually leaves that region. Colloid 9 travels into the convergence zone near the contact point in 16-bead layer, and comes very close to the glass-bead surface, but it was not captured. The above suggests that the convergence zone near the contact point is likely the preferred site for colloid attachment.

Fig. 11(b) shows 10 colloid trajectories within a y–z slice defined by $79\delta \le x \le 81\delta$. This slice contains the centers of the glass beads in the 9-beads layers. In this case, colloids (1,2,9,10) can travel very easily near the channel walls due to large local porosity. Away from the wall regions, the trajectories are similar to Fig. 11(a).

The colloid trajectories shown in the two slices in Fig. 11 are mostly two-dimensional because the two slices are located in region of high local porosity (larger than the mean porosity) as illustrated in Fig. 12. Fig. 11(a) corresponds to 295 μm $\le x \le$ 305 μm and Fig. 11(b) for 395 μm $\le x \le$ 405 μm.

Fig. 13 shows 10 trajectories within a y–z slice defined by $71\delta \le x \le 73\delta$. In this slice, glass beads in 16-beads (or 9-beads) layers do not touch one another, but glass beads in the 16-beads layer are in contact with those in the 9-beads layer. The range of interception radii is $0.760R$ to $0.835R$ for the 16-beads layer, and $0.893R$ to $0.937R$ for the 9-beads layer.

[1] Before we arrived at this result, we tested convergence of the results with changing time step size. In the process, we found that too large of a time step could lead to deposition simply due to a numerical artifact: an overprediction of colloid velocity near a grain surface can lead to unstable oscillations of colloid position, first outside the peak energy barrier; then the oscillations amplified and led to a jump across the peak energy barrier which became counted as a deposition at PEM. Such numerical artifact is more severe when the local hydrodynamic interactions are considered — this is expected as the correction factors are very sensitive function of gap distance when the gas distance is small. The results presented here used a very small time step size of $dt = \tau_c^*/2,000$. Physically, such small time step size is needed only when a colloid is very close to the grain surface (say below 100 nm) where the correction factors and the DLVO energy profile changes very rapidly. Outside this region, a larger time step size can be used. We are currently investigating the use of variable time step size for Lagrangian tracking of colloids. For this reason, the deposition rate observed in our previous 2D study [5] was contaminated by this numerical artifact.

Author's personal copy

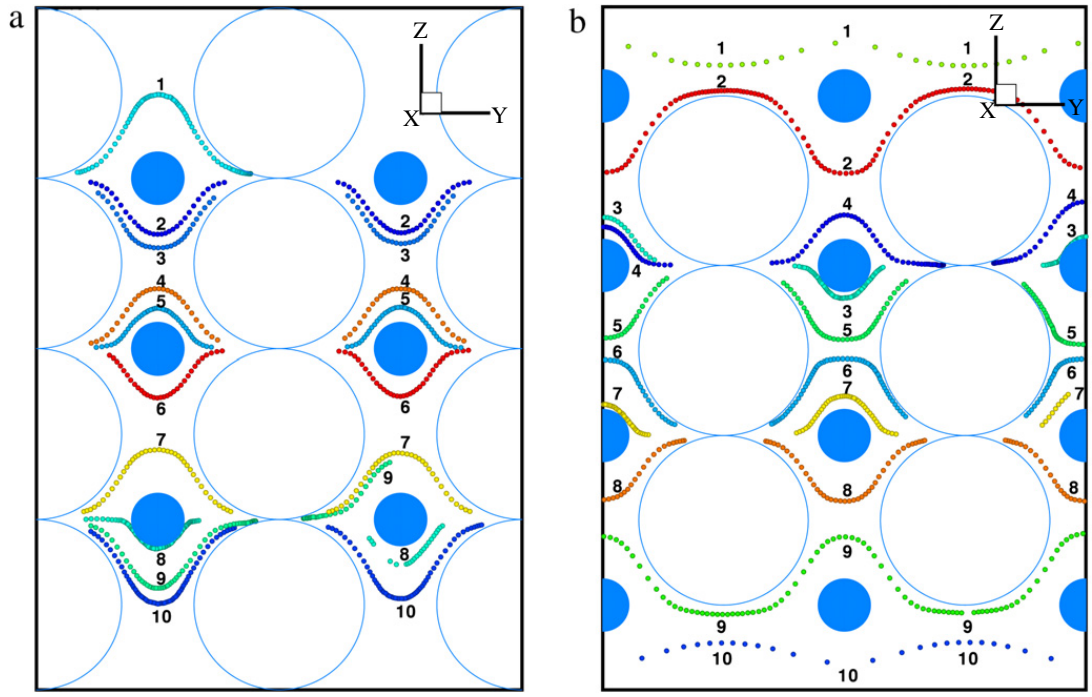

Fig. 11. 3D trajectories seen within a narrow 2D slice of thickness 10 μm: (a) for a slice with $59\delta \leq x \leq 61\delta$, where glass beads in the 16-beads layer contact each other; (b) for a slice with $79\delta \leq x \leq 81\delta$, where glass beads in the 9-beads layer contact each other.

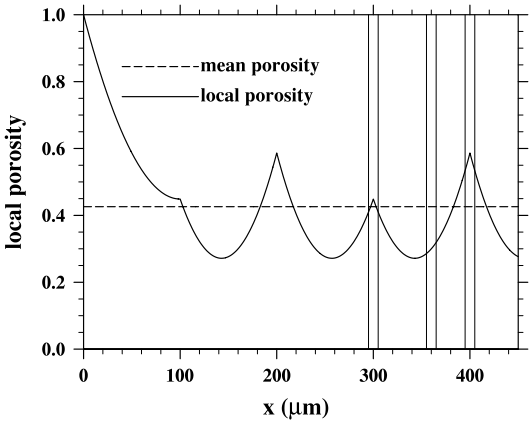

Fig. 12. Local porosity as a function of x. The three pairs of vertical lines mark the slices considered in Figs. 11 and 13.

There is a strong cross flow (relative to the streamwise flow velocity) in this slice due to the layer–layer contact blocking, so colloids do not stay very long in this slice, rather they wander in and out of this slice frequently. Note that the average porosity (0.300) in this slice is lower than the mean porosity (0.426). The slice is also shown in Fig. 12, we note that the porosity increases with x locally so the cross flow tends to be directed to the positive x direction (out of the paper).

The above pore-scale visualizations do not provide any details on the motion of colloids near a grain surface. Furthermore, Brownian motion does not show up since the motion caused by the fluid flow dominates the trajectories visualized at the pore scale in Figs. 11 and 13. Next, we shall probe into the region in the grain surface. Fig. 14 shows two representative trajectories, using a deposited colloid from Run 1 and Run 2. The gap distance from the grain surface is plotted as a function of time. Several important observations can be made here. First, since these two deposited colloids happened to be injected at an exact same location, their trajectories are similar initially. At about $h_{\text{gap}} = 1100\ nm \approx 2a_c$, the effect of hydrodynamic retardation started to separate the two trajectories, with hydrodynamic retardation slows down the approach to the grain surface. This is seen clearly by the different slopes of the two trajectories. Second, the fluctuations are caused by the Brownian motion. A close examination reveals that the fluctuations are reduced as the colloids make its way to the surface, this reduction of the level of fluctuations is also due to the hydrodynamic retardation effect — a drag larger than the Stokes drag causes a smaller movement of the colloid when hit by thermal fluctuation force. In the Eulerian approach when the concentration is solved, the hydrodynamic retardation decrease the effective diffusion coefficient, as seen in the study of Yang et al. [40]. Third, right before deposition, the approach speed is increased due to increased van der Waals force near the SEM well. Finally, Fig. 14(b) shows the time evolution of gap distance after the colloids are captured by the SEM well. Colloids

Author's personal copy

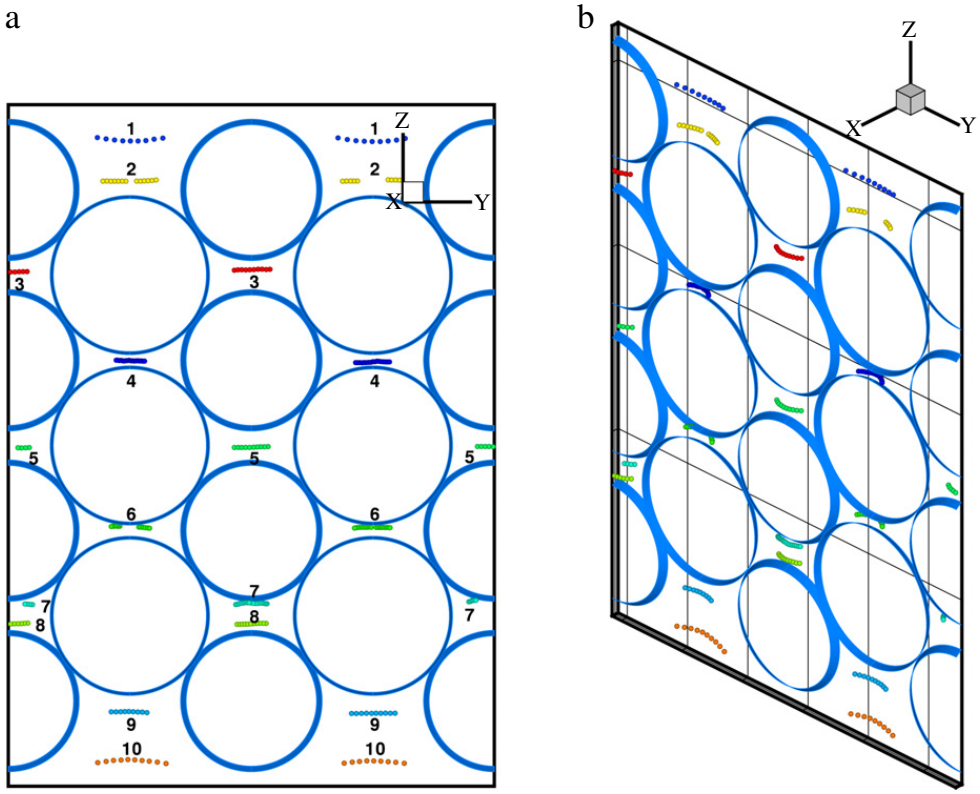

Fig. 13. 3D trajectories seen within a narrow 2D slice of thickness 10 μm for a slice with $71\delta \leq x \leq 73\delta$: (a) 2D view; (b) 3D view.

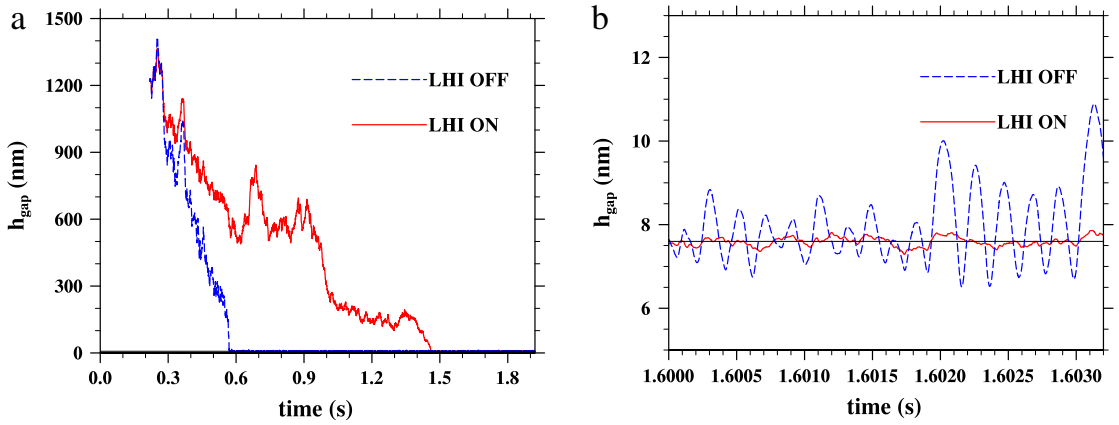

Fig. 14. Gap distance between a colloid and a collector surface as a function of time: (a) from the moment of release to the SEM deposition; (b) a zoom-in view after the capture of colloids by SEM well. The horizontal line represents the SEM location of 7.58 nm at the given ionic strength of 0.1 M.

can move around the SEM due to Brownian energy, but cannot escape the SEM well as the depth of SEM well is −15.25 kT. Interestingly, without the hydrodynamic retardation, the trajectory shows a quasi-periodic oscillation with a time period of about 2×10^{-4} s or about $0.3125\tau_c^*$. This period is roughly 625 time steps, so it must have been fully resolved. Qualitatively, we may expect a physical oscillation around SEM as the DLVO force changes direction there, if the viscous drag (the damping) is weak. We will show this is the case below.

Fig. 15 shows the drag force, DLVO force, and Brownian force for the same colloid from Run 2 discussed in Fig. 14(b) after the capture by SEM. Brownian force is by far the most dominant force. Due to its short time scale and large relative magnitude, Brownian force is plotted only for a small time duration in Fig. 15(b). The drag force shows intermediate magnitude and time scale of oscillation, showing that colloids frequently change its velocity direction. We note that the drag force shown in Fig. 15 is about a factor 5 larger than the drag force experienced by colloids when they are in the inner pore region (i.e., flow region not very close to the grain surface), due to the significant augmentation by local hydrodynamic interaction, although the relative velocity between the colloid and the flow in the inner pore region is much larger. The DLVO force only depends on location, having the smallest magnitude and longest time scale of oscillation. The above picture clearly shows that Brownian motion is the driving force for the random motion after the capture.

Author's personal copy

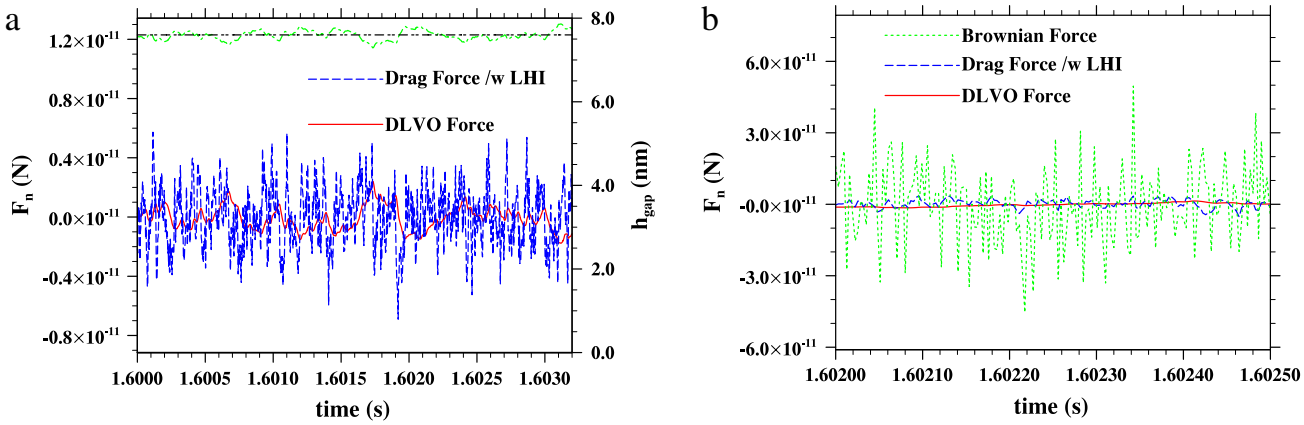

Fig. 15. Forces acting on a colloid with LHI after the capture by the SEM well: (a) drag force and physicochemical force as a function of time, and the corresponding gap distance; (b) a zoom-in portion of (a), including drag force, physicochemical force, and Brownian force.

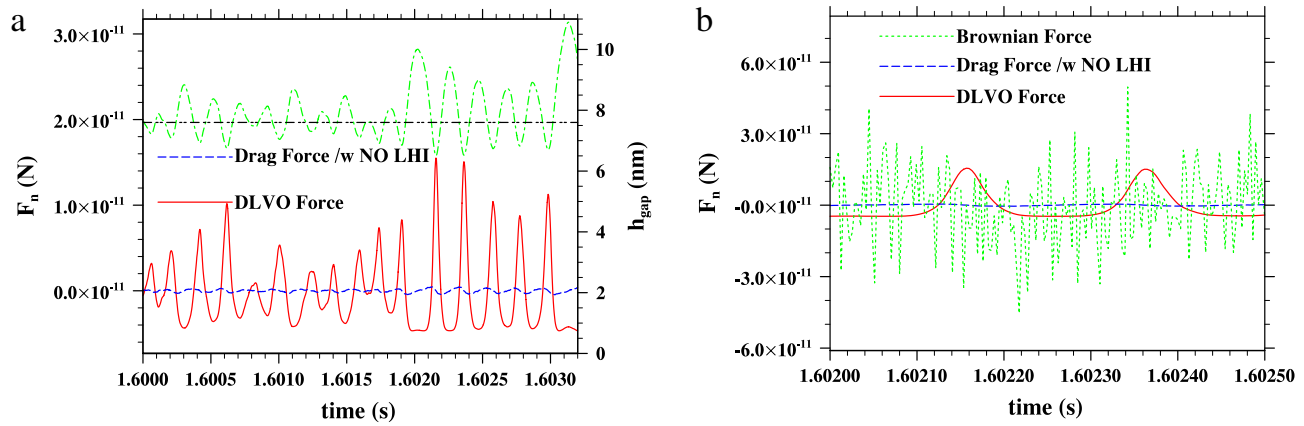

Fig. 16. Forces acting on a colloid without LHI after the capture by the SEM well: (a) drag force and physicochemical force as a function of time, and the corresponding gap distance; (b) a zoom-in portion of (a), including drag force, physicochemical force, and Brownian force.

Finally, Fig. 16 shows the drag force, DLVO force, and Brownian force for the same colloid from Run 1 discussed in Fig. 14(b) after the capture by SEM. In this case, without the hydrodynamic retardation, the colloid can move more freely around SEM, the DLVO force becomes comparable in magnitude as the Brownian force, and the drag force which acts as damping is negligible. This then implies that the system can oscillate with a period on the order of $T = 2\pi\sqrt{(\tau_c^*/(3.125 \times 10^5))/(kU_s)} \approx 7.87 \times 10^{-4}\sqrt{k}$, where $k\zeta U_s$ is the spring constant corresponding to the local average slope shown in Fig. 10(b) near SEM. An estimate from Fig. 10(b) for k is $k = 15\zeta U_s$ (N/nm). Then the period of the oscillation is $T = 2.03 \times 10^{-4}$ s, precisely the period observed in Fig. 14(b).

4. Conclusions and summary

This paper reports preliminary results on microscopic viscous flow simulation in a three-dimensional porous channel and on the transport of sub-micron colloids in a model porous medium. We apply simultaneously two fundamentally different numerical methods to solve viscous flows in a porous channel with different levels of porosity and grain–grain contact. For a porous channel with one fixed spherical grain, the two methods yielded identical velocity profiles and mean flow statistics, force and torques on the grain. When two grains are introduced with both grain–grain and grain–channel walls contact points, a reasonable inter-comparison is also achieved. These cases could serve as benchmark cases for future numerical methods of three-dimensional flows in complex geometry.

As the numbers of grains and contact points are increased, it appears that the mesoscopic LBM approach is superior than the hybrid macroscopic approach. The numerical implementation of the no-slip boundary condition on grain surface is simpler in LBM, and the results of the simulated flow are more accurate near the contact points. In LBM, the calculation of all fluid–surface interaction forces are straightforward and the overall integral force balance was shown to be better satisfied. It may be possible that our Physalis code could be further improved to reach the similar consistency and accuracy as LBM.

Transport and deposition of colloids were simulated by Lagrangian tracking, under a given solution ionic strength and physicochemical setting. No deposition at the primary energy minimum was found, but depositions at the secondary energy minimum were demonstrated. The local hydrodynamic retardation appears to reduce the ability for colloids to move into

Author's personal copy

the SEM well, but does not prevent this to occur. Visualizations of colloid trajectories within thin slices show different levels of complexity depending on the local porosity, flow convergence, and contact points. The trajectories are quasi-two-dimensional when the local porosity is high. A close examination of colloid motion near the surface clearly shows the effect of local hydrodynamic interaction in delaying the approach of a colloid to a collector surface due to van der Waals attraction. After the colloids being captured by the SEM well, a colloid may exhibit an quasi-periodic motion if the local hydrodynamic interaction is not considered, due to a relative weak drag force. The period of such oscillation can be predicted in terms of particle inertia and directional change of DLVO force near SEM, based on a simple mass–spring oscillator model. Hydrodynamic interaction appears to introduce high enough dissipation to eliminate such quasi-periodic motion. It was shown that a very small time step size is needed when a colloid is close to the grain surface to correctly account for the rapid change in DLVO force and the local hydrodynamic retardation effect.

We are in the process of performing a more careful analysis of the concentration profile near grain surface and using our simulation tool to study depth-dependent retention profile and time-dependent effluent concentration profile (i.e., the breakthrough curve). These will allow us to compare our simulation results to those in the previous computational studies. Future work also includes consideration of random grain packing and inter-comparison with our parallel microscopic visualization experiments, as well as consideration of grains with irregular shapes.

Acknowledgements

This study is supported by the US Department of Agriculture (NRI-2006-02551, NRI-2008-02803), US National Science Foundation (ATM-0527140), and National Natural Science Foundation of China (Project No. 10628206). LPW acknowledges the travel support provided by ICMMES-08 through the NSF grant BET 0827259. The authors thank Dr. V.I. Lazouskaya and Dr. J. Han for the helpful discussions on the general topic of colloidal transport in both the saturated and the unsaturated soil.

References

[1] S.A. Bradford, S. Torkzaban, S.L. Walker, Coupling of physical and chemical mechanisms of colloid straining in saturated porous media, Water Res. 41 (2007) 3012–3024.
[2] W.P. Johnson, X. Li, G. Yal, Colloid retention in porous media: Mechanistic confirmation of wedging and retention in zones of flow stagnation, Environ. Sci. Technol. 41 (2007) 1279–1287.
[3] C. Shen, B. Li, Y. Huang, Y. Jin, Kinetics of coupled primary- and secondary-minimum deposition of colloids under unfavorable conditions, Environ Sci. Technol. 41 (2007) 6976–6982.
[4] H. Gao, J. Han, Y. Jin, L.-P. Wang, Modeling microscale flow and colloid transport in saturated porous media, Int. J. Comp. Fluid Dyn. 22 (2008) 493–505.
[5] Q.M. Qiu, J. Han, H. Gao, L.-P. Wang, Y. Jin, Pore-scale investigations of flow speed and ionic strength on colloid deposition in saturated media, Langmuir, 2009 (submitted for publication).
[6] S.A. Bradford, N. Toride, A stochastic model for colloid transport and deposition, J. Environ. Qual. 36 (2007) 1346–1356.
[7] C.J. van Oss, Interfacial Forces in Aqueous Media, Marcel Dekker, New York, 1994.
[8] R. Rajagopalan, C. Tien, Trajectory analysis of deep-bed filtration with the sphere-in-cell porous media model, AIChE J. 22 (1976) 523–533.
[9] S. Kim, S.J. Karrila, Microhydrodynamics, Principles and Selected Applications, Butterworth-Heinemann, Boston, 1991.
[10] J. Happel, Viscous flow in multiparticle systems: Slow motion of fluids relative to beds of spherical particles, AIChE J. 4 (1958) 197–201.
[11] A.C. Payatakes, R. Rajagopalan, C. Tien, On the use of Happel's model for filtration studies, J. Colloid Interf. Sci. 49 (1974) 321–325.
[12] A.C. Payatakes, C. Tien, R.M. Turian, Trajectory calculation of particle deposition in deep bed filtration, AIChE J. 20 (1974) 889–899.
[13] C.A. Paraskeva, V.N. Burganos, A.C. Payatakes, Three dimensional trajectory analysis of particle deposition in constricted tubes, Chem. Eng. Comm. 108 (1991) 23–48.
[14] V.N. Burganos, C.A. Paraskeva, P.D. Christofides, A.C. Payatakes, Motion and deposition of non-Brownian particles in upflow collectors, Sep. Technol. 4 (1994) 47–54.
[15] R.S. Cushing, D.F. Lawler, Depth filtration: Fundamental investigation through three-dimensional trajectory analysis, Environ. Sci. Technol. 32 (1998) 3793–3801.
[16] Z. Zhang, A. Prosperetti, A second-order method for three-dimensional particle simulation, J. Comp. Phys. 210 (2005) 292–324.
[17] D. d'Humières, I. Ginzburg, K. Krafczyk, P. Lallemand, L.-S. Luo, Multiple-relaxation-time lattice Boltzmann models in three dimensions, Phil. Trans. Roy. Soc. London A. 360 (2002) 437–451.
[18] Z. Guo, C. Zheng, B. Shi, Discrete lattice effects on the forcing term in the lattice Boltzmann method, Phys. Rev. E. 65 (2002) 046308.
[19] L.-P. Wang, B. Afsharpoya, Modeling fluid flow in fuel cells using the lattice-Boltzmann approach, Math. Comput. Simulation 72 (2006) 242–248.
[20] P. Lallemand, L.-S. Luo, Theory of the lattice Boltzmann method: Acoustic and thermal properties in two and three dimensions, Phys. Rev. E. 68 (2003) 036706.
[21] P. Lallemand, L.-S. Luo, Lattice Boltzmann method for moving boundaries, J. Comp. Phys. 184 (2003) 406–421.
[22] I. Ginzburg, F. Verhaeghe, D. d'Humiéres, Two-relaxation-time lattice Boltzmann scheme: About parametrization, velocity, pressure and mixed boundary conditions, Commun. Comput. Phys. 3 (2008) 427–478.
[23] I. Ginzburg, F. Verhaeghe, D. d'Humiéres, Study of simple hydrodynamic solutions with the two-relaxation-times lattice Boltzmann scheme, Commun. Comput. Phys. 3 (2008) 519–581.
[24] D. Yu, R. Mei, L.-S. Luo, W. Shyy, Viscous flow computations with the method of lattice Boltzmann equation, Progr. Aerosp. Sci. 39 (2003) 329–367.
[25] Z. Zhang, A. Prosperetti, A method for particle simulation, J. Appl. Mech. Trans. ASME 70 (2003) 64–74.
[26] H. Gao, L.-P. Wang, Towards fully resolved simulation of turbulent collision of heavy particles, CDROM Proceedings of the 6th International Conference on Multiphase Flow, Paper 713, Leipzig, Germany, July 9–17, 2007.
[27] D.L. Brown, R. Cortez, M.L. Minion, Accurate projection methods for the incompressible Navier–Stokes equations, J. Comp. Phys. 168 (2001) 464–499.
[28] J. Kim, P. Moin, Application of a fractional-step method to incompressible Navier–Stokes equations, J. Comp. Phys. 59 (1985) 308–323.
[29] M.R. Maxey, J.J. Riley, Equation of motion for a small rigid sphere in a nonuniform flow, Phys. Fluids 26 (1983) 883–889.
[30] L.A. Spielman, Particle capture from low-speed laminar flows, Annu. Rev. Fluid Mech. 9 (1977) 297–319.
[31] M.J. Elimelech, J. Gregory, X. Jia, R.A. Williams, Particle Deposition and Aggregation: Measurement, Modeling, and Simulation, Butterworth-Heinemann, Oxford, 1995.
[32] L. Landau, E. Lifshitz, Fluid Mechanics, Addison-Wesley, London, 1959.

Author's personal copy

[33] A.J.C. Ladd, Short-time motion of colloidal particles: Numerical simulation via a fluctuating lattice-Boltzmann equation, Phys. Rev. Lett. 70 (1993) 1339–1342.
[34] A.J.C. Ladd, Numerical simulations of particulate suspensions via a discretized Boltzmann equation. Part 1. Theoretical foundation, J. Fluid Mech. 271 (1994) 285–309; Part 2. Numerical results, J. Fluid Mech. 271 (1994) 311–339.
[35] B. Dünweg, U.D. Schiller, A.J.C. Ladd, Statistical mechanics of the fluctuating lattice Boltzmann equation, Phys. Rev. E. 76 (2007) 036704.
[36] C.J. van Oss, Interfacial Forces in Aqueous Media, Marcel Dekker, New York, 1994.
[37] B.V. Derjaguin, L. Landau, Theory of the stability of strongly charged lyophobic sols and of the adhesion of strongly charged particles in solutions of electrolytes, Acta Physicochem (USSR) 14 (1941) 633–662.
[38] E.J. Verwey, J.T.G. Overbeek, Theory of Stability of Lyophobic Colloids, Elsevier, Amsterdam, 1948.
[39] R. Hogg, T.W. Healy, D.W. Fuerstenau, Mutual coagulation of colloidal dispersions, Trans. Faraday Soc. 62 (1966) 1638–1651.
[40] C. Yang, T. Dabros, D. Li, J.H. Masliyah, Kinetics of particle transport to a solid surface from an impinging jet under surface and external force fields, J. Colloid Int. Sci. 208 (1998) 226–240.